# Synthetic Tailoring of Ionic Conductivity in Multicationic Substituted, High-Entropy Lithium Argyrodite Solid Electrolytes

Jing Lin, Mareen Schaller, Gennady Cherkashinin, Sylvio Indris, Jianxuan Du, Clemens Ritter, Aleksandr Kondrakov, Jürgen Janek, Torsten Brezesinski,* and Florian Strauss*

Superionic conductors are key components of solid-state batteries (SSBs). Multicomponent or high-entropy materials, offering a vast compositional space for tailoring properties, have recently attracted attention as novel solid electrolytes (SEs). However, the influence of synthetic parameters on ionic conductivity in compositionally complex SEs has not yet been investigated. Herein, the effect of cooling rate after high-temperature annealing on charge transport in the multicationic substituted lithium argyrodite $Li_{6.5}[P_{0.25}Si_{0.25}Ge_{0.25}Sb_{0.25}]S_5I$ is reported. It is demonstrated that a room-temperature ionic conductivity of ~12 mS cm$^{-1}$ can be achieved upon cooling at a moderate rate, superior to that of fast- and slow-cooled samples. To rationalize the findings, the material is probed using powder diffraction, nuclear magnetic resonance and X-ray photoelectron spectroscopy combined with electrochemical methods. In the case of moderate cooling rate, favorable structural (bulk) and compositional (surface) characteristics for lithium diffusion evolve. $Li_{6.5}[P_{0.25}Si_{0.25}Ge_{0.25}Sb_{0.25}]S_5I$ is also electrochemically tested in pellet-type SSBs with a layered Ni-rich oxide cathode. Although delivering larger specific capacities than $Li_6PS_5Cl$-based cells at high current rates, the lower (electro)chemical stability of the high-entropy Li-ion conductor led to pronounced capacity fading. The research data indicate that subtle changes in bulk structure and surface composition strongly affect the electrical conductivity of high-entropy lithium argyrodites.

## 1. Introduction

Increasing demands for fast charging, high-energy-density rechargeable batteries have pushed academic and industrial research towards solid-state battery (SSB) design.[1,2] From a materials perspective, this is pursued through the development of improved cathode, anode and solid electrolyte (SE) materials.[3,4] Apart from the challenge of utilizing lithium-metal anodes and designing a stable interface between the cathode active material (CAM) and the superionic SE, a key requirement for achieving advanced SSBs is the use of (electro)chemically stable and mechanically soft ion conductors. In this regard, lithium thiophosphates represent a major class of promising SEs, as they offer high ionic conductivities and are mechanically soft. The latter allows for intimate contact with the active electrode material(s), which in turn helps reducing detrimental (chemo)mechanical effects during cell cycling.[5–7]

Particularly lithium argyrodites with the general formula $Li_6PS_5X$ (with X = Cl, Br or

J. Lin, J. Du, A. Kondrakov, J. Janek, T. Brezesinski, F. Strauss
Battery and Electrochemistry Laboratory (BELLA)
Institute of Nanotechnology (INT)
Karlsruhe Institute of Technology (KIT)
Hermann-von-Helmholtz-Platz 1
76344 Eggenstein-Leopoldshafen, Germany
E-mail: torsten.brezesinski@kit.edu; florian.strauss@kit.edu

M. Schaller, S. Indris
Institute for Applied Materials–Energy Storage Systems (IAM-ESS)
Karlsruhe Institute of Technology (KIT)
Hermann-von-Helmholtz-Platz 1
76344 Eggenstein-Leopoldshafen, Germany

G. Cherkashinin
Advanced Thin Film Technology
Institute of Materials Science
Technical University of Darmstadt
Alarich-Weiss Str. 2, 64287 Darmstadt, Germany

C. Ritter
Institut Laue-Langevin
Grenoble Cedex 9 38042, France

A. Kondrakov
BASF SE
Carl-Bosch-Str. 38, 67056 Ludwigshafen, Germany

I) were subject of intense SE development. Over the years, their ionic conductivity could be increased beyond 10 mS cm$^{-1}$ through substitution on the P and/or X site.[8–13] Substitutions typically increase the $S^{2-}/X^-$ site inversion and/or modify the lithium sublattice, which can lead to high ion mobility.[10,12,14,15] Apart from improving ionic conductivity in crystalline solids by iso- or aliovalent substitutions in the host lattice,[14–17] the temperature profile used in the solid-state synthesis, i.e., the annealing temperature and especially the cooling rate, can also have a profound effect on the resulting charge-transport properties. For instance, fast cooling via immersing the sample in liquid nitrogen immediately after annealing can stabilize high-temperature polymorphs or point defects at room temperature[18–24] or freeze the $S^{2-}/X^-$ site inversion in the case of $Li_6PS_5Br$ and $Li_{5.5}PS_{4.5}Cl_{1.5}$ (possibly leading to enhanced conductivity).[25–27] When it comes to high-entropy (compositionally complex) lithium-ion conductors, the effect of annealing temperature and cooling rate in general has not yet been thoroughly investigated.

For high-entropy materials (HEMs), which are characterized by a $\Delta S_{conf} > 1.5R$ (with $\Delta S_{conf}$ representing the configurational entropy), the emergence of new and/or improved properties has been reported.[28–30] Various HEMs including oxides, sulfides and carbides have been synthesized and employed, among others, as battery materials, catalysts or thermoelectrics.[31,32] Recently, this concept has been transferred to ceramic ion conductors, and some promising materials crystallizing in garnet, rock salt or Na SuperIonic CONDuctor (NASICON)-type structures have been reported.[33–37] However, their (electro)chemical assessment is sparse, and very high ionic conductivities could so far only be achieved for multicationic and -anionic substituted sulfide-based SEs.[36,38,39] Depending on the elemental composition, the entropy contribution may compete with (destabilizing) positive mixing enthalpies $\Delta H_{mix}$. This is particularly critical at low temperatures. While a uniform solid solution may be achieved at elevated temperatures during synthesis, the entropy term may become too small during cooling, leading to demixing depending on the cooling conditions. Whether demixing has a negative effect on ionic conductivity is unclear, and it surely depends on the type of demixing, i.e., if spinodal decomposition occurs or nucleation is required during the demixing process.

In view of these considerations, herein we report on the investigation into how the temperature profile, in particular the cooling rate after high-temperature annealing, affects the ionic conductivity in a multicationic substituted (high-entropy) lithium argyrodite. We demonstrate that altering the cooling rate in the synthesis of $Li_{6.5}[P_{0.25}Si_{0.25}Ge_{0.25}Sb_{0.25}]S_5I$ has indeed a profound effect on conductivity. We find that the maximum ionic conductivity is achieved when the sample is cooled at a moderate rate. Using a combination of structure and charge-transport characterization techniques, the crystalline lattice is found to be relatively robust against different cooling rates, however it exhibits

J. Janek
Institute of Physical Chemistry & Center for Materials Research (ZfM/LaMa)
Justus-Liebig-University Giessen
Heinrich-Buff-Ring 17, 35392 Giessen, Germany

unique characteristics that enable high ionic conductivity. In addition, X-ray photoelectron spectroscopy (XPS) revealed a surface composition that deviates from the original stoichiometry but appears to be beneficial for charge transport. Finally, the as-synthesized SE was tested in pelletized SSBs and compared to the commonly used argyrodite $Li_6PS_5Cl$. Because of the much higher ionic conductivity of the high-entropy material, larger cell capacities were obtained, especially at high C-rates. Yet, the lower (electro)chemical stability of $Li_{6.5}[P_{0.25}Si_{0.25}Ge_{0.25}Sb_{0.25}]S_5I$ than $Li_6PS_5Cl$ led to a stronger capacity decay during cycling.

## 2. Results and Discussion

Inorganic superionic conductors consisting of a compositionally complex rigid host structure and a defective lithium sublattice (with mobile ions) may be highly sensitive to the synthesis procedure, i.e., annealing temperature and cooling rate. Regarding the synthesis of lithium argyrodites, temperatures ranging from ≈300 to 550 °C with dwell times ranging from a few hours to days are usually applied in the annealing step. However, incorporating a high-energy milling step prior to heating can strongly reduce the required annealing time and induce crystallization, and is even more crucial in the case of compositionally complex materials for ensuring uniform mixing of precursors/elements. Here, stoichiometric amounts of precursors were mixed by ball milling at a relatively low speed, and differential scanning calorimetry (DSC) measurements were performed to reveal potential crystallization and decomposition temperatures (Figure S1a, Supporting Information). Based on the DSC results, three different annealing temperatures, namely 400, 500 and 550 °C, were tested. The corresponding X-ray diffraction (XRD) patterns indicated that 500 °C leads to negligible $Li_2S$ and LiI impurity phase formation (Figure S1b,c, Supporting Information). Moreover, the material obtained at 500 °C exhibited the highest room-temperature ionic conductivity (in cold-pressed state) among the different samples (10.7 mS cm$^{-1}$, see Table S1, Supporting Information). Therefore, an annealing temperature of 500 °C was selected for any further experiments.

A schematic presentation of the synthesis protocol used and the respective temperature profile are depicted in **Figure 1**a. After the first precursor mixing step (1 h at 250 rpm), the milling speed was increased to 450 rpm, and milling was continued for another 10 h. Subsequently, the recovered powder was pelletized, annealed for 10 h and thereafter cooled at three different rates, namely fast cooling via quenching in liquid nitrogen, moderate (medium) cooling over a time of ≈1.5 h (5 °C min$^{-1}$) and slow cooling over ≈48 h (10 °C h$^{-1}$), which is referred to as Q, MC and SC, respectively, hereafter. As can be seen from the XRD patterns in Figure 1b, the high-energy milling step already induced crystallization of the argyrodite phase. This is commonly observed in the literature for non-high-entropy lithium argyrodites.[40–42] A small crystallite size can be expected considering the broad reflections. To improve crystallinity of the material, pelletized samples were annealed in vacuum-sealed quartz ampules for 10 h at 500 °C. At first glance, no major differences in the patterns were noticed (Figure 1b). To probe the crystal structure, the samples were subjected to high-resolution neutron powder diffraction (NPD) at 298 and 10 K (to minimize atomic displacement), followed by Rietveld refinement analysis.

**ADVANCED
SCIENCE NEWS**

www.advancedsciencenews.com

NANO · MICRO

**small**

www.small-journal.com
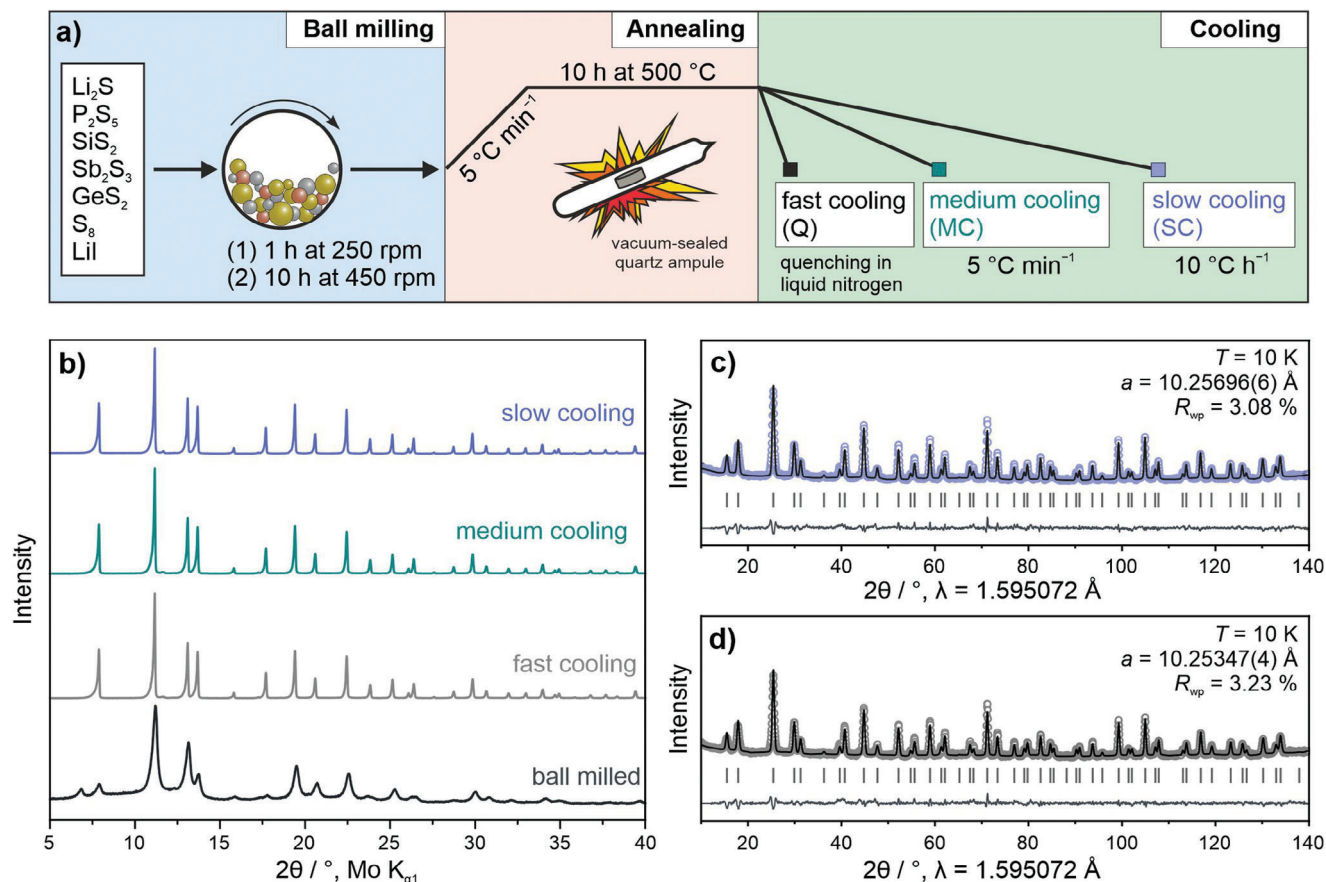
**Figure 1.** Synthesis and structural characterization of $Li_{6.5}[P_{0.25}Si_{0.25}Ge_{0.25}Sb_{0.25}]S_5I$. a) Schematic illustration of the synthesis pathway including milling and annealing, followed by one of the three chosen cooling rates. b) XRD patterns for the ball-milled precursor mixture and samples prepared with different cooling rates. c,d) NPD patterns and corresponding Rietveld plots at $T = 10$ K for slow- and fast-cooled samples. The open circles and black and gray lines represent the observed, calculated and difference profiles, respectively. Expected Bragg reflections are indicated by vertical ticks.

The Rietveld profiles for the Q and SC samples measured at $T = 10$ K are exemplarily shown in Figure 1c,d. The patterns could be indexed in the $F−43m$ space group with very similar lattice parameter of $a = 10.25696(6)$ Å (SC) and $10.25347(4)$ Å (Q) ($a = 10.24932(5)$ Å for the MC sample, see Table S2, Supporting Information). The structural parameters from Rietveld analysis are given in Table S3–S6 (Supporting Information) and ref. [36].

The calculated crystal structure of $Li_{6.5}[P_{0.25}Si_{0.25}Ge_{0.25}Sb_{0.25}]S_5I$ is depicted in **Figure 2**a. The $S^{2−}$ and $I^−$ ions form a face-centered cubic anion sublattice (Wyckoff positions $4a$ and $4d$), and in addition, $S^{2−}$ ions are located in half of the tetrahedral voids ($16e$) around the multicationic substituted octahedral sites ($4b$), forming $[P_{0.25}Si_{0.25}Ge_{0.25}Sb_{0.25}]S_4^{3.5−}$ polyanions. In fact, such mixed polyanions constitute a combination of individual $[PS_4]^{3−}$, $[SiS_4]^{4−}$, $[GeS_4]^{4−}$ and $[SbS_4]^{3−}$ species, which are evenly
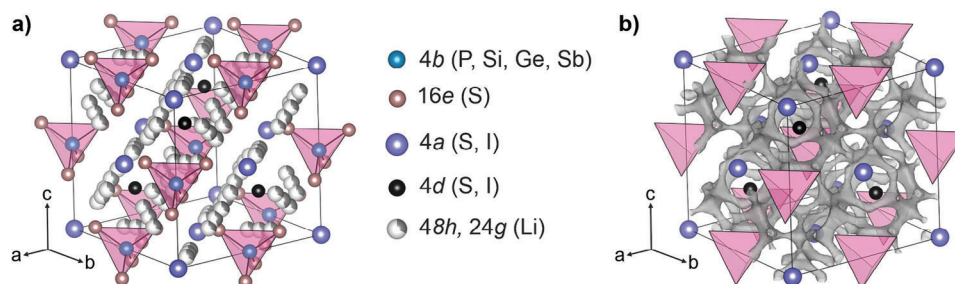


**Figure 2.** Crystal structure of $Li_{6.5}[P_{0.25}Si_{0.25}Ge_{0.25}Sb_{0.25}]S_5I$. a) Schematic view with the different Wyckoff positions and their elemental constituents indicated in the legend on the right. b) Bond-valence energy landscape revealing the 3D lithium diffusion pathways (gray trajectories). For clarity, only atoms on the $4a$ and $4d$ sites are shown. $[P_{0.25}Si_{0.25}Ge_{0.25}Sb_{0.25}]S_4^{3.5−}$ polyanions are depicted as pink tetrahedra.

**ADVANCED
SCIENCE NEWS**

www.advancedsciencenews.com
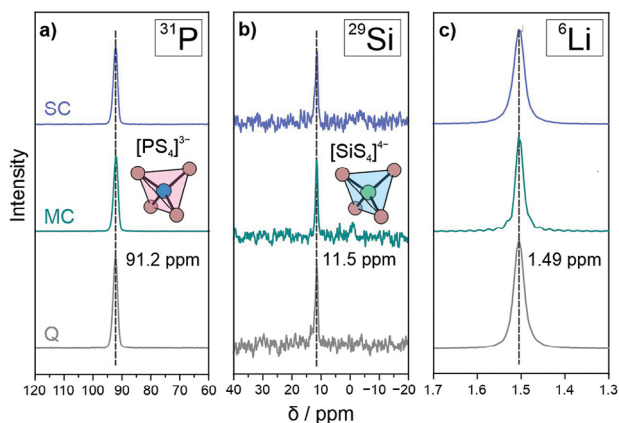
**NANO · MICRO**

**small**

www.small-journal.com

**Figure 3.** Sulfide-based tetrahedral polyanions revealed by MAS NMR spectroscopy. a) $^{31}$P, b) $^{29}$Si and c) $^{6}$Li spectra collected from the $Li_{6.5}[P_{0.25}Si_{0.25}Ge_{0.25}Sb_{0.25}]S_5I$ samples prepared with different cooling rates (Q, MC and SC refer to fast, medium and slow cooling, respectively).

distributed throughout the lattice. Moreover, in the argyrodite structure, $S^{2-}$ (4$d$) and $I^-$ (4$a$) anions are known to mix over the respective Wyckoff positions ($S^{2-}/X^-$ site inversion). We found a site inversion of $\approx$13% for the Q and SC samples, compared to 12% for the MC sample, among the highest values reported in the literature for $S^{2-}/I^-$ mixing. Analysis of the NPD data also provided detailed structural information on the lithium sublattice. The Li atoms usually form Frank-Kasper polyhedra around the 4$d$ site, expressed in two Wyckoff positions, namely 48$h$ and 24$g$,[8] thereby producing 3D lithium diffusion pathways (Figure 2b). For the Q sample, it was found that 70 and 30% of Li is located on 48$h$ and 24$g$, respectively, at room temperature. Upon reducing the cooling rate, the Li occupancy on the 48$h$ site is lowered to 62 and 60% for MC and SC, respectively (Figure S2a, Supporting Information). We note that the occupancies remained virtually unaltered at 10 K. Surprisingly, a slight increase in Li situated on the 24$g$ site was observed with decreasing cooling rate, which can be regarded as an intermediate/transition site. Therefore, the opposite trend might be expected, meaning quenching the sample should lead to increased Li occupancy on 24$g$. This counterintuitive finding seems to be a result of the large lattice distortions prevailing in high-entropy lithium argyrodites. The slightly varying Li occupancies also led to somewhat different Li-Li jump distances, with the intercage jump distance being an important structural parameter in determining the long-range lithium-diffusion characteristics (Figure S2b, Supporting Information). At room temperature, this distance was smallest for the MC sample [3.24(2) Å, compared to 3.28(3) and 3.25(3) Å for Q and SC, respectively, see Table S7, Supporting Information). Naturally, all Li-Li distances were lower upon cooling to 10 K.

To further corroborate the presence of $[PS_4]^{3-}$ and $[SiS_4]^{4-}$ tetrahedra within the $Li_{6.5}[P_{0.25}Si_{0.25}Ge_{0.25}Sb_{0.25}]S_5I$ structure and reveal the presence of potential amorphous impurities (invisible from diffraction data), $^{31}$P, $^{29}$Si and $^{6}$Li magic-angle spinning (MAS) nuclear magnetic resonance (NMR) spectroscopy measurements were carried out. The respective spectra are shown in **Figure 3**. A distinct peaks at 91.2 ppm was observed for $^{31}$P for all samples (Figure 3a), indicative of phosphorus being in a $[PS_4]^{3-}$

(tetrahedral) environment and consistent with the chemical shift found for other lithium thiophosphates.[35,36,43–45] It should be noted that, compared to $Li_6PS_5I$, the $^{31}$P signal was shifted by $\approx$5 ppm, which is probably due to the unique chemical environment around the $[P_{0.25}Si_{0.25}Ge_{0.25}Sb_{0.25}]S_4^{3.5-}$ tetrahedra.[8] Regarding the $^{29}$Si signal, a distinct peak located at 11.5 ppm was observed in all cases (Figure 3b), evidencing the presence of $[SiS_4]^{4-}$ species, in agreement with literature results.[36,43] In the $^{6}$Li MAS NMR data (Figure 3c), a peak at 1.49 ppm appeared, similar to other lithium argyrodites.[9,45,46] Overall, comparable spectra with no signs of impurity contributions were obtained for the samples prepared with different cooling rates. This again demonstrates the minor effect that cooling rate has on the average/local crystal structure and further verifies the robustness of the high-entropy argyrodite lattice.

The local structure of the $[GeS_4]^{4-}$ tetrahedra was studied by Ge K-edge transmission X-ray absorption spectroscopy (XAS) measurements conducted on the MC sample and a $GeS_2$ reference material. Extended X-ray absorption fine structure (EXAFS) spectra [$k^2$-weighted $\chi$(k)] and the corresponding magnitudes of the Fourier transform are shown in Figure S3a–c (Supporting Information). The $|\chi(R)|$ peak for both the $Li_{6.5}[P_{0.25}Si_{0.25}Ge_{0.25}Sb_{0.25}]S_5I$ and $GeS_2$ is located at $R \approx$ 1.65 Å, indicating the presence of $[GeS_4]^{4-}$ tetrahedra.[47]

To gain information on the oxidation state of the elements and possible differences in near-surface composition, XPS measurements were carried out. The respective binding energies from curve fitting are given in Table S8 (Supporting Information). For the Sb 3d core-level region, only the $3d_{5/2}$ components are shown (**Figure 4**a–c) due to the large spin-orbit splitting ($\approx$9.3 eV). For all samples, the Sb $3d_{5/2}$ spectrum is superimposed by the O 1s signal at a binding energy of $\approx$532 eV. The asymmetry of the Sb $3d_{5/2}$ line indicates two different oxidation states, with peaks centered at 530.3 and 529.4 eV. They can be assigned to $Sb^{5+}$ and $Sb^{3+}$, respectively, in a Sb-S chemical environment, originating from the presence of $[SbS_4]^{3-}$ structural motifs and $Sb^{3+}$ surface impurities.[36,48–50] The asymmetric O 1s line also points toward at least two chemical states, which can most likely be attributed to oxygenated Si, Sb, P and/or Ge. However, clear assignment is challenging. The S 2p detail spectra are depicted in Figure 4d–f, with the main contribution at 161.4 eV evidencing the presence of sulfide species, in agreement with literature data.[36,51–53] In addition, a minor S 2p component is evident at 163.5 eV, which is usually ascribed to polysulfide impurities.[54] Figure 4g–i shows the P 2p core-level region, revealing a doublet peak at 132.2 eV for all samples characteristic of the $[PS_4]^{3-}$ units.[36,51,55,56] The Si 2p data are centered at $\approx$101 eV, and again, they are virtually identical for the different samples (Figure 4j–l). The major component can be assigned to $[SiS_4]^{4-}$, in agreement with reports available in the literature,[57,58] while the minor component at 102.6 eV lies in between the binding energies usually detected for $[SiS_4]^{4-}$ and $SiO_2$. It can thus be correlated with partially oxygenated $SiO_x$ surface impurities.[36,57–60] The I 4d region ($\approx$2.0 eV spin-orbit splitting) is depicted in Figure 4m–o. The presence of $I^-$ is apparent from the characteristic contributions, with the major one at $\approx$49 eV and the minor one centered $\approx$0.5 eV higher in binding energy. It has been hypothesized that these contributions stem from two different crystallographic environments in the structure (4$a$ and 4$d$ sites).[36] The Ge 3d and
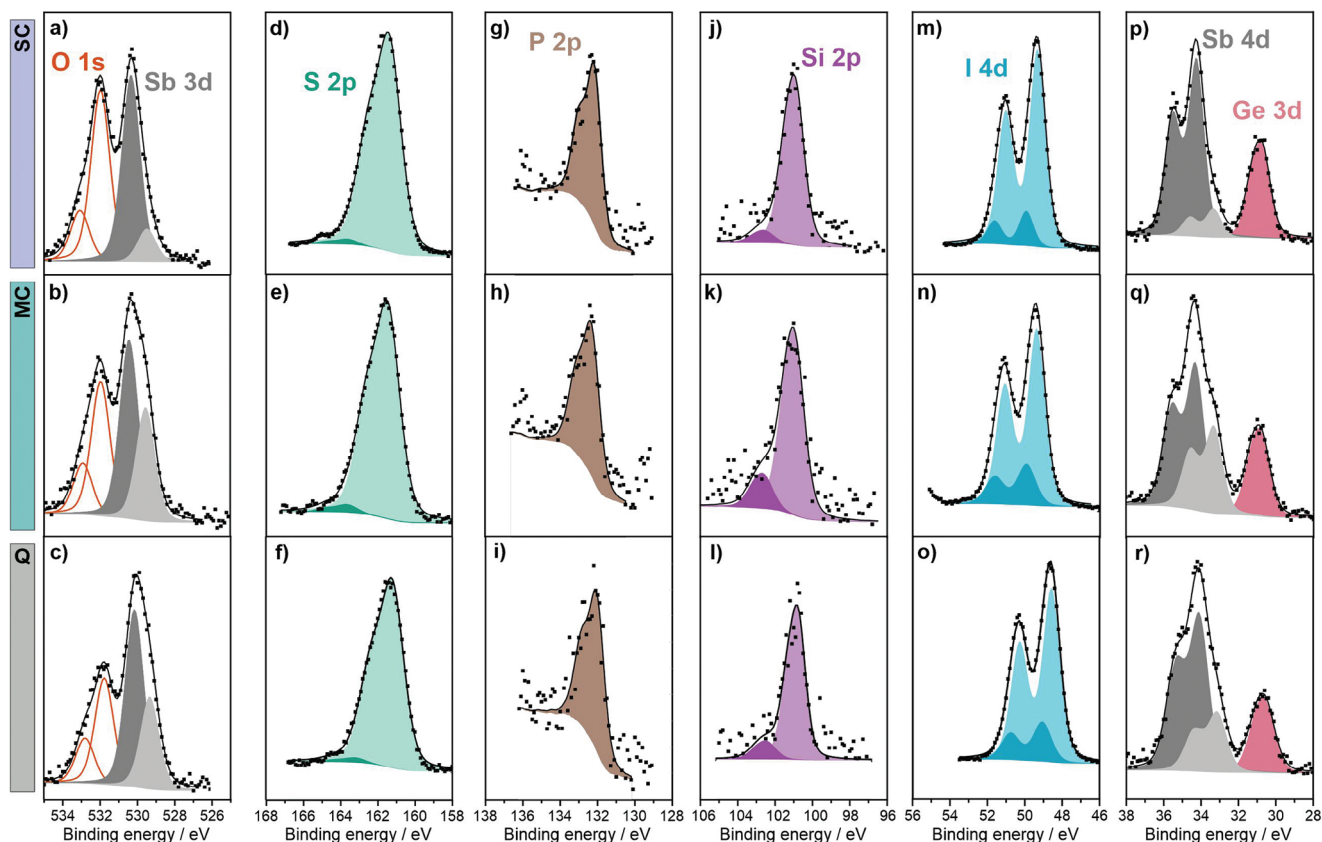
**ADVANCED
SCIENCE NEWS**

www.advancedsciencenews.com

NANO · MICRO

**small**

www.small-journal.com

**Figure 4.** Effect of cooling rate on surface composition of $Li_{6.5}[P_{0.25}Si_{0.25}Ge_{0.25}Sb_{0.25}]S_5I$ probed using XPS. High-resolution a–c) Sb $3d_{5/2}$ and O 1s, d–f) S 2p, g–i) P 2p, j–l) Si 2p, m–o) I 4d and p–r) Sb 4d and Ge 3d photoelectron spectra collected from samples prepared with different cooling rates (Q, MC and SC refer to fast, medium and slow cooling, respectively). Black dots and solid lines represent the experimental data and curve-fitting results, respectively.

Sb 4d regions are shown in Figure 4p–r. The Sb 4d peaks comprise two contributions, at ≈34.3 and 33.2 eV, confirming the presence of $Sb^{5+}$ and $Sb^{3+}$, respectively, at the near-surface regions of the samples. In addition, the Ge 3d spectra (≈30.8 eV) seem to indicate the presence of a single component (corresponding to $[GeS_4]^{4-}$).[48,61] Taken together, the spectra collected from the samples prepared with different cooling rates were found to be very similar for the S 2p, P 2p, I 4d and Ge 3d core levels. However, the data also revealed increased $Sb^{3+}$ (contribution at 529.4 eV) and $SiO_x$ (contribution at 102.6 eV) contents for the MC sample.

To visualize the complex surface composition of $Li_{6.5}[P_{0.25}Si_{0.25}Ge_{0.25}Sb_{0.25}]S_5I$, scanning transmission electron microscopy (STEM) imaging combined with energy-dispersive X-ray spectroscopy (EDX) was used. As shown in **Figure 5**, particles in the micrometer size range were observed. The corresponding elemental maps revealed uniform distributions on the nanoscale. As expected, oxygen was also found on the particle surface, in agreement with the oxygenated species detected by XPS (see Figure 4a–c,j–l). According to quantitative XPS analysis, the concentration of surface oxygen was much lower than that of sulfur (Table S9, Supporting Information). However,
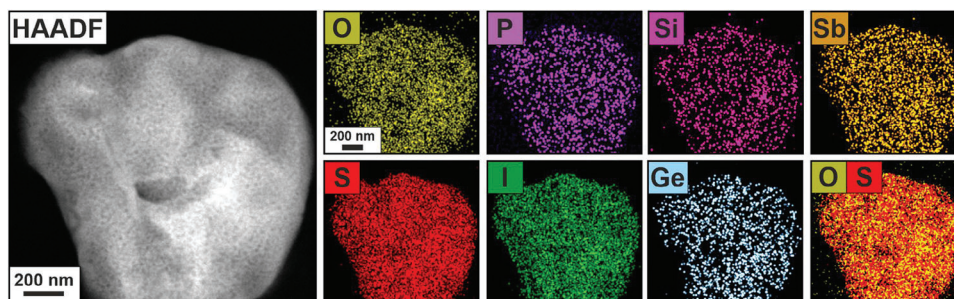


**Figure 5.** Results from STEM-EDX imaging/mapping. A representative high-angle annular dark field (HAADF) image and corresponding elemental maps from EDX are shown.
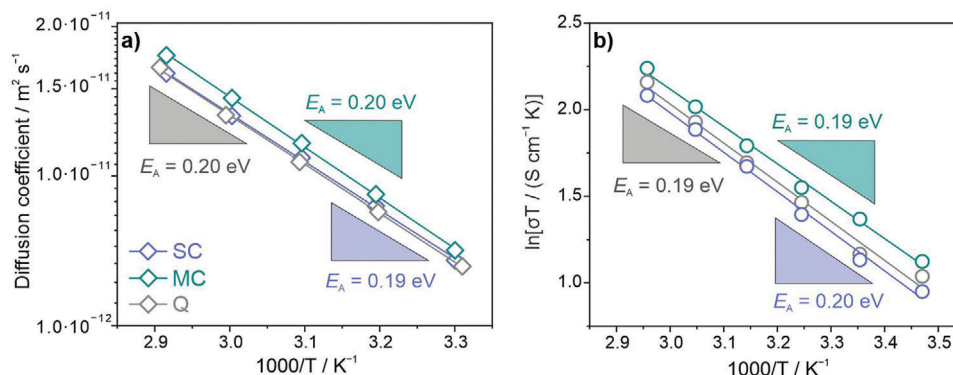
**Figure 6.** Charge-transport properties of $Li_{6.5}[P_{0.25}Si_{0.25}Ge_{0.25}Sb_{0.25}]S_5I$ determined by a) $^7Li$ PFG NMR spectroscopy and b) EIS. a) Arrhenius plot of the diffusion coefficient and b) conductivity versus reciprocal temperature for the samples prepared with different cooling rates. The activation energies are indicated. If error bars are not visible, the standard deviation is smaller than the symbol.

when the cooling rate was very low, a slight increase in oxygen content was noticed (for the SC sample). Overall, the oxygen signals from XPS and STEM-EDX can be clearly assigned to surface impurity formation, despite the fact that the materials were strictly handled under inert atmosphere.

After having revealed similar bulk and surface structural characteristics for the $Li_{6.5}[P_{0.25}Si_{0.25}Ge_{0.25}Sb_{0.25}]S_5I$ prepared with different cooling rates, the Li-ion dynamics were probed in the temperature range of 30–70 °C using $^7Li$ pulsed field gradient (PFG) NMR spectroscopy (Figure S4, Supporting Information). In so doing, diffusion coefficients of $D_{Li} = 6.58 \cdot 10^{-12}$ m² s⁻¹ (Q), $7.09 \cdot 10^{-12}$ m² s⁻¹ (MC) and $6.77 \cdot 10^{-12}$ m² s⁻¹ (SC) were determined at 30 °C, which are on the same order of magnitude to that of other highly conducting lithium thiophosphates.[9,36,45,46,62,63] Arrhenius plots of diffusivity against reciprocal temperature are shown in **Figure 6**a. Virtually identical activation energies of $E_A = 0.20$, 0.20 and 0.19 eV were determined from the slopes (assuming Arrhenius-type temperature dependence) for Q, MC and SC, respectively.

The electrical conductivities were determined by electrochemical impedance spectroscopy (EIS) measurements conducted on sintered pellets with ion-blocking electrodes between 15 and 65 °C. The corresponding Nyquist plots of the electrochemical impedance only revealed a capacitive tail, indicating high ionic conductivity (Figure S5, Supporting Information). Room-temperature conductivities of 11.9 (±0.39), 12.3 (±0.70) and 11.0 (±0.57) mS cm⁻¹ were calculated for Q, MC and SC, respectively, and very similar activation energies of $E_A = 0.19$ (Q), 0.19 (MC) and 0.20 eV (SC) were determined from the corresponding Arrhenius plots (Figure 6b). As can be seen, they agree well with the $^7Li$ PFG NMR results.

Using the Nernst-Einstein equation, the ionic conductivities were also estimated from the diffusion coefficients. A summary of the EIS and $^7Li$ PFG NMR results is given in **Table 1** and further depicted in **Figure 7**a. From the data, it is evident that the ionic conductivities determined by $^7Li$ PFG NMR are lower by ≈2 mS cm⁻¹. This difference between EIS and $^7Li$ PFG NMR is presumably rooted in the contribution of (favorable) grain-boundary conduction, as EIS probes the overall specimen conductivity unlike $^7Li$ PFG NMR (only bulk transport properties are probed). However, a similar trend in conductivity with cooling

**Table 1.** Summary of the Li-ion conductivities ($\sigma_{ion}$) at $T = 298$ K and corresponding activation energies ($E_A$) from temperature-dependent EIS and $^7Li$ PFG NMR spectroscopy measurements..

| Sample | $\sigma_{ion}$ / mS cm⁻¹ [EIS] | $E_A$ / eV [EIS] | $\sigma_{ion}$ / mS cm⁻¹ [PFG NMR] | $E_A$ / eV [PFG NMR] |
|---|---|---|---|---|
| Quenching (Q) | 11.9 ± 0.39 | 0.19 ± 0.01 | 9.12 ± 0.05 | 0.20 ± 0.01 |
| Medium cooling (MC) | 12.3 ± 0.70 | 0.19 ± 0.01 | 10.9 ± 0.04 | 0.20 ± 0.01 |
| Slow cooling (SC) | 11.0 ± 0.57 | 0.20 ± 0.01 | 9.12 ± 0.05 | 0.19 ± 0.01 |

rate is apparent from both techniques. This means that the conductivity of $Li_{6.5}[P_{0.25}Si_{0.25}Ge_{0.25}Sb_{0.25}]S_5I$ (MC) is indeed higher than that of the Q and SC samples. No significant influence of the cooling rate on activation energy was found.

To further assess the transport properties of the $Li_{6.5}[P_{0.25}Si_{0.25}Ge_{0.25}Sb_{0.25}]S_5I$ samples, their electronic conductivity was determined by DC polarization measurements to be $3.83 \cdot 10^{-5}$, $3.18 \cdot 10^{-7}$ and $1.23 \cdot 10^{-5}$ S cm⁻¹ for Q, MC and SC, respectively. Interestingly, MC was found to exhibit two orders of magnitude lower electronic conductivity than the Q and SC samples (Figure 7b). We assume that this is related to the surface composition and presence of impurities. The fact that the electronic conductivity is orders of magnitude higher than that of other Li-ion conductors seems to be due, in part, to the intrinsic properties of high-entropy lithium argyrodites.[9,46,64]

SSBs with lithium thiophosphate SEs typically make use of cold-pressed materials. For that reason, the conductivity of the different samples was also determined in a cold-pressed state. As expected, the resulting ionic conductivities were somewhat lower than those of sintered pellets. Nevertheless, high room-temperature conductivities of 7.4 (±0.4), 10.9 (±0.25) and 5.5 (±0.15) mS cm⁻¹ were found by EIS for Q, MC and SC, respectively, following a similar trend to the sintered pellets (Figure 7b). As mentioned above, this means that the MC sample indeed shows superior ionic conductivity over Q and SC and sintering helps to achieve better grain contact, thereby minimizing grain-boundary contributions.
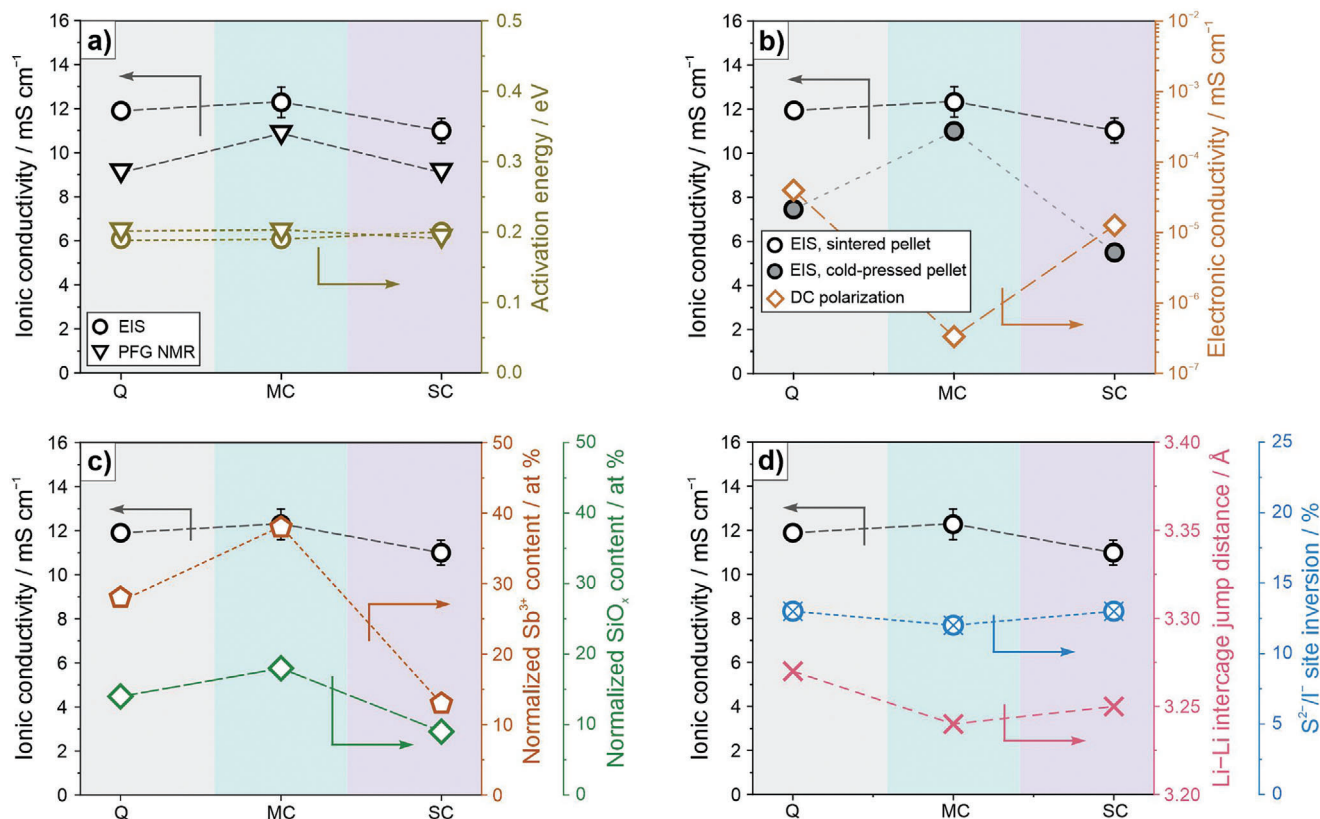
**ADVANCED
SCIENCE NEWS**

www.advancedsciencenews.com

**NANO · MICRO
small**

www.small-journal.com

**Figure 7.** Bulk structure/surface composition-charge transport property relationships. a) Ionic conductivities and activation energies determined by EIS and $^7$Li PFG NMR spectroscopy. b) Comparison of ionic conductivities measured on sintered and cold-pressed pellets and electronic conductivities determined from DC polarization measurements (on sintered pellets) for the $Li_{6.5}[P_{0.25}Si_{0.25}Ge_{0.25}Sb_{0.25}]S_5I$ samples prepared with different cooling rates. c) Normalized $Sb^{3+}$ and $SiO_x$ contents from XPS and d) Li-Li intercage jump distances and $S^{2-}/I^-$ site inversions shown together with the ionic conductivities. If error bars are not visible, the standard deviation is smaller than the symbol. Dashed lines are for eye guidance only.

From a surface composition point of view, it is found that increasing amounts of $Sb^{3+}$ and $SiO_x$ species correlate with increasing ionic conductivity and decreasing electronic conductivity (Figure 7c). Hence, slight changes in surface composition apparently can exert a substantial impact on the conductivity of polycrystalline materials. In this regard, it is important to note that enhanced interfacial ion transport is a well-known phenomenon[65,66] and might play a role here as well. For example, $Sb_2S_3$ (with $Sb^{3+}$) is a poor electronic conductor,[67,68] which agrees with our finding that an increasing $Sb^{3+}$ (surface) fraction leads a strong decrease in electronic conductivity. From a structural perspective, the short Li-Li intercage jump distances (Figure 7d), together with favorable surface/grain-boundary composition, are likely responsible for fast lithium transport in the MC sample. These results collectively show that, in addition to favorable bulk structural features, the surface composition strongly affects the overall ionic conductivity. However, little attention has been paid to this in the context of sulfide-based SEs until now.

Finally, the electrochemical behavior of the best-conducting SE sample (MC) was tested in pellet-type SSBs with a $LiNbO_3$-coated $LiNi_{0.85}Co_{0.1}Mn_{0.05}O_2$ (NCM851005) cathode and an indium-lithium anode and compared to that of commercially available argyrodite $Li_6PS_5Cl$. Initially, the cells were cycled at a C/10

rate and 25 °C, followed by ex situ EIS measurements. For the $Li_{6.5}[P_{0.25}Si_{0.25}Ge_{0.25}Sb_{0.25}]S_5I$, first-cycle specific charge and discharge capacities of 237 and 182 mAh g$^{-1}$ were achieved, which translates to 77% Coulomb efficiency (referred to as CE in the following, see **Figure 8**a). In the case of $Li_6PS_5Cl$, the cells delivered a lower charge but higher discharge capacity, with $q_{ch} = 221$ mAh g$^{-1}$ and $q_{dis} = 190$ mAh g$^{-1}$, corresponding to a CE of 86%. The ≈10% difference in CE upon using the multicomponent SE suggests a lower (electro)chemical stability compared to the $Li_6PS_5Cl$. However, the impedance spectra revealed a larger charge-transfer resistance for $Li_6PS_5Cl$ (Figure 8b). Fitting of the data allowed determining the different contributions to the overall impedance (Figure S6, Supporting Information), namely bulk SE ($R_{bulk}$), SE grain boundary ($R_{GB}$), CAM/SE ($R_{CAM/SE}$) and anode/SE ($R_{anode/SE}$). The $R_{GB}$ was found to be 15.5 Ω (12.2 Ω cm$^2$) for $Li_6PS_5Cl$ and only 3.4 Ω (2.7 Ω cm$^2$) for $Li_{6.5}[P_{0.25}Si_{0.25}Ge_{0.25}Sb_{0.25}]S_5I$, presumably due to favorable grain-boundary conduction as discussed above. For the $R_{CAM/SE}$ and $R_{anode/SE}$, values of 78.9 Ω (61.9 Ω cm$^2$)/6.6 Ω (5.2 Ω cm$^2$) and 4.7 Ω (3.7 Ω cm$^2$)/27.1 Ω (21.3 Ω cm$^2$) were obtained for $Li_6PS_5Cl$ and the high-entropy SE, respectively. Interestingly, the $R_{CAM/SE}$ showed the opposite trend to the first-cycle CE, which was significantly lower for $Li_{6.5}[P_{0.25}Si_{0.25}Ge_{0.25}Sb_{0.25}]S_5I$. We assume that, despite more severe degradation, the charge transport through

**ADVANCED
SCIENCE NEWS**

www.advancedsciencenews.com

NANO · MICRO

**small**

www.small-journal.com

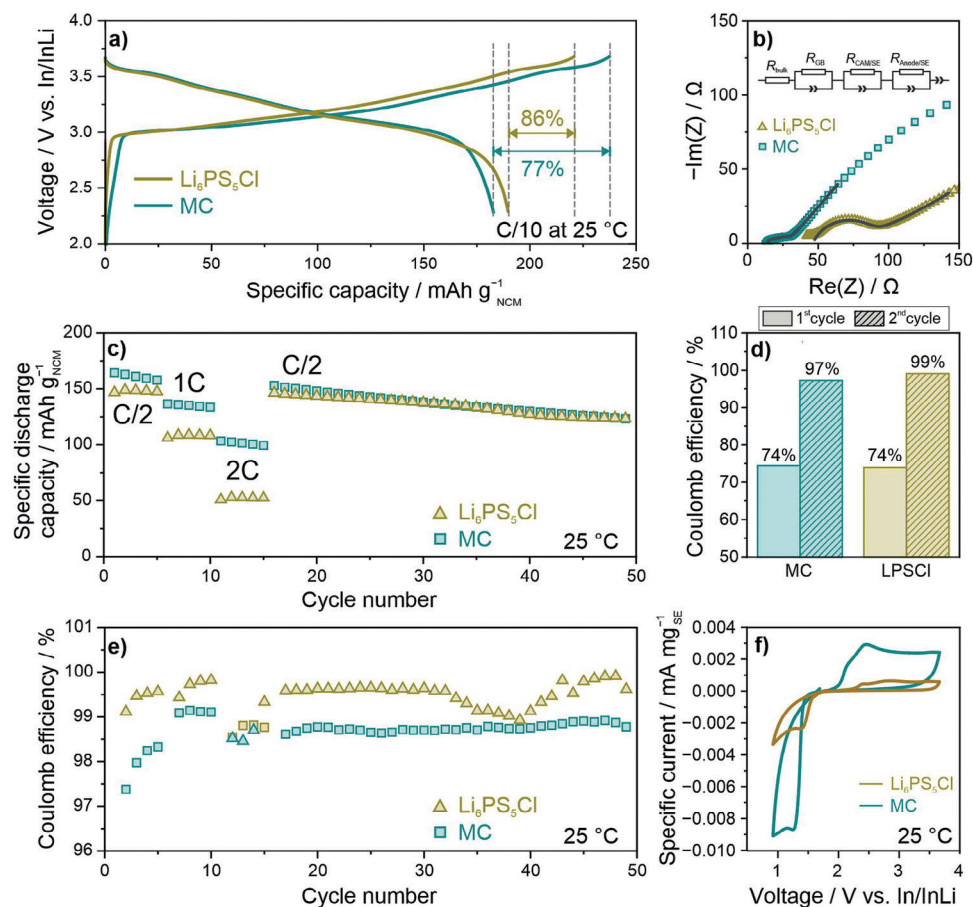**Figure 8.** (Electro)chemical testing of bulk-type SSBs. a) Initial voltage profiles of cells containing either the $Li_{6.5}[P_{0.25}Si_{0.25}Ge_{0.25}Sb_{0.25}]S_5I$ (MC) or commercial argyrodite $Li_6PS_5Cl$ SE at C/10 rate and 25 °C. b) Impedance spectra collected after the first cycle shown in a). c) Rate capability and long-term cycling performance. d) Coulomb efficiencies for the first two and e) following cycles. f) First-cycle CV curves for mixtures of SE and carbon black as working electrode. Data are averaged from two identical cells.

the cathode interface(s) is facilitated, which is directly reflected in the impedance spectra.

Next, the SSB cells were subjected to rate capability and long-term performance testing. To this end, the galvanostatic cycling was conducted at 25 °C and C-rates ranging from C/2 to 2C (Figure 8c; Figure S7a, Supporting Information). For $Li_{6.5}[P_{0.25}Si_{0.25}Ge_{0.25}Sb_{0.25}]S_5I$, first-cycle specific charge and discharge capacities of 226 and 168 mAh g$^{-1}$ were achieved at C/2, corresponding to an initial CE of 74% (Figure 8d). In contrast, the $Li_6PS_5Cl$-based cells delivered lower capacities of $q_{ch} = 198$ mAh g$^{-1}$ and $q_{dis} = 147$ mAh g$^{-1}$, leading to a similar CE of 74%. Notable is the large overpotential of the $Li_6PS_5Cl$-based cells (increased by ≈250 mV compared to the high-entropy SE, see differential capacity plots in Figure S7b, Supporting Information). This increase in overpotential is probably due to the lower room-temperature ionic conductivity of $Li_6PS_5Cl$ (≈2 mS cm$^{-1}$ versus 11–12 mS cm$^{-1}$). After five cycles, the C-rate was first increased to 1C and then to 2C. As can be seen from the data for the high-entropy SE, specific discharge capacities of ≈135 and 101 mAh g$^{-1}$ were achieved at 1C and 2C, respectively. For $Li_6PS_5Cl$, the drop in discharge capacity with increasing current rate was much more pronounced, with $q_{dis} ≈ 109$ mAh g$^{-1}$ at

1C and 53 mAh g$^{-1}$ at 2C. This result can be explained by the significantly higher ionic conductivity of the high-entropy SE, which is capable of better accommodating high current densities (2C ≈ 4.4 mA cm$^{-2}$). Subsequently, the cells were cycled at C/2 and found to undergo virtually linear capacity decay, with $q_{dis} ≈ 123$ mAh g$^{-1}$ in the 49th cycle, corresponding to an overall capacity loss of 27% and 16% (relative to the initial discharge capacity) for $Li_{6.5}[P_{0.25}Si_{0.25}Ge_{0.25}Sb_{0.25}]S_5I$ and $Li_6PS_5Cl$, respectively. This difference in capacity retention provides evidence for the lower electrochemical stability of the multicomponent SE, for which possible decomposition phases (interfacial degradation products) have recently been identified by XPS.[36] Although the initial CE (C/2 rate) was similar for both SEs tested, it was lower for the high-entropy material during subsequent cycling (Figure 8e). After an increase over the first five cycles, the CE stabilized below 99% for $Li_{6.5}[P_{0.25}Si_{0.25}Ge_{0.25}Sb_{0.25}]S_5I$ but above 99.5% for $Li_6PS_5Cl$, corroborating the above conclusions. This further implies that the as-formed decomposition interphase is kinetically unstable, leading to continuous SE degradation, which might be associated with the increased electronic conductivity. Interestingly, a bump in the CE data between cycles 30 and 40 was noticed for $Li_6PS_5Cl$, which is

**ADVANCED
SCIENCE NEWS**

www.advancedsciencenews.com

NANO · MICRO

**small**

www.small-journal.com

not mirrored in the specific discharge capacities in Figure 8c. This has repeatedly been reported in the literature and assigned to (chemo)mechanically-driven cell degradation.[51,69,70] However, in the case of the $Li_{6.5}[P_{0.25}Si_{0.25}Ge_{0.25}Sb_{0.25}]S_5I$, it did not occur, and we assume that this is because of the different softness of the SEs (Young's modulus). Note that increasing compositional complexity typically causes a lowering of the Young's modulus.[71]

To determine the (electro)chemical stability window of both materials and deconvolute anodic and cathodic stability issues, cyclic voltammetry (CV) measurements were conducted on mixtures of SE and carbon black as working electrode. Figure 8f shows the first-cycle CV curves, which reveal larger currents in the anodic and cathodic scans for $Li_{6.5}[P_{0.25}Si_{0.25}Ge_{0.25}Sb_{0.25}]S_5I$. This again confirms the lower stability of the high-entropy SE (exhibiting a relatively narrow electrochemical stability window). With further cycling (Figure S8, Supporting Information), a strong decrease in the absolute reductive (cathodic) current was noticed for both SEs, while the oxidative (anodic) current only changed marginally in the case of the high-entropy SE.

Overall, the CV data agree with the results from galvanostatic cycling, indicating the formation of a kinetically unstable decomposition interphase that does not effectively prevent SE degradation during battery operation.

## 3. Conclusion

In summary, we have examined the impact of the synthesis procedure, especially annealing temperature and cooling rate, on structure-charge transport property relationships in the multicationic substituted $Li_{6.5}[P_{0.25}Si_{0.25}Ge_{0.25}Sb_{0.25}]S_5I$ SE. As reported in the past for ceramic Li-ion conductors, the synthesis procedure/conditions may have a profound effect on ionic conductivity, however clear trends have yet to be established. In the case of $Li_6PS_5Br$, this has been attributed to increased $S^{2-}/Br^-$ site inversion with fast sample cooling via quenching in liquid nitrogen, i.e., site-disorder freezing.[25–27] For the material studied in this work, we found that the cooling rate after a given high-temperature anneal indeed affects the ionic conductivity. For medium cooling, an increase in conductivity over fast- and slow-cooled samples was observed. To understand the origin of this result, the bulk crystal structure was probed using XRD and NPD in combination with MAS NMR spectroscopy. For the medium-cooled sample, the shortest Li-Li intercage jump distances and a high degree of $S^{2-}/I^-$ site inversion (12-13%) were found. Apart from these for ion mobility favorable bulk structural characteristics, the surface composition was also investigated via XPS and STEM-EDX. Small differences among the samples were noticed, in particular the presence of increased amounts of $Sb^{3+}$ and $SiO_x$ surface impurities for the medium-cooled material. It can be assumed that the unique surface composition also affects, at least to some degree, the conductivity. Overall, it seems that the high ionic conductivity of the $Li_{6.5}[P_{0.25}Si_{0.25}Ge_{0.25}Sb_{0.25}]S_5I$ SE is mainly due to a combination of advantageous bulk and surface structural/compositional features. However, the bulk crystal structure was found to be less susceptible to temperature effects than the surface (composition). The findings further emphasize that classical synthetic approaches to optimize ionic conductivity in ceramic ion conductors may not be transferable to compositionally complex SEs.

Because of the high room-temperature ionic conductivity, the MC sample was also tested in pellet-type SSBs and the performance compared to that achieved with $Li_6PS_5Cl$. The high-entropy SE cells were capable of delivering larger specific discharge capacities at high current rates but suffered from more pronounced (electro)chemically-driven degradation, leading to faster performance decay. The data clearly demonstrate that the conductivity in lithium argyrodite SEs can be synthetically tailored, however their stability seems to be lower than that of $Li_6PS_5Cl$. This indicates that achieving high ionic conductivity is not the only challenge but other metrics, such as (electro)chemical stability and mechanical behavior, need to be considered too. Taken together, high-entropy SEs provide a vast compositional space that is not limited to sulfide-based materials, thereby maximizing the opportunity to improve several key performance indicators of SSBs by compositional design.

## 4. Experimental Section

*General*: If not stated otherwise, all work steps were performed under inert atmosphere, and the precursors were used as received.

*Synthesis*: A stoichiometric mixture of $Li_2S$ (99.99%, Sigma-Aldrich), $P_2S_5$ (99%, Sigma-Aldrich), $GeS_2$ (99.9%, Goodfellow), $SiS_2$ (99.99%, Goodfellow), $Sb_2S_3$ (99.99%, Alfa Aesar) and LiI (99.999%, Sigma-Aldrich) plus 10 wt.% excess sulfur (99.99%, Sigma-Aldrich) was weighed into a 70 mL zirconia milling jar. Next, 20 zirconia milling balls with a diameter of 10 mm were added, and the mixture was milled for 1 h at 250 rpm, followed by 10 h at 450 rpm. The resulting powder was pressed into pellets ($\approx$300 mg, 10 mm diameter) at 3 t and vacuum sealed in quartz ampules ($10^{-3}$ bar). To avoid trace water, the ampules were dried at 500 °C using a heat gun under dynamic vacuum ($10^{-3}$ bar) prior to use. The samples were then annealed at 500 °C for 10 h at a heating rate of 5 °C min$^{-1}$ and cooled down at different rates: (1) Quenching in liquid $N_2$, (2) 5 °C min$^{-1}$ or (3) 10 °C h$^{-1}$. During the initial survey of the optimal temperature, the samples were prepared as described above and annealed at 450, 500 or 550 °C for 10 h with heating and cooling rates set to 5 °C min$^{-1}$.

*Differential Scanning Calorimetry*: Measurements were performed at a heating rate of 5 °C min$^{-1}$ using a NETZSCH DSC 204 F1 Phoenix. To this end, the samples were sealed in alumina crucibles under Ar atmosphere.

*Laboratory X-ray Diffraction*: The samples were sealed in borosilicate capillaries (0.68 mm inner diameter and 0.01 mm wall thickness, Hilgenberg) under Ar atmosphere and subjected to XRD analysis using a STOE Stadi-P diffractometer with a DECTRIS MYTHEN 1K strip detector in Debye-Scherrer geometry. The instrument utilizes a Mo anode to generate X-rays of wavelength $\lambda = 0.70926$ Å.

*Neutron Powder Diffraction*: For NPD, cylindrical vanadium containers of diameter 6 mm were filled with $\approx$2 g of sample. The measurements were performed at the D2B high-resolution powder diffractometer located at the Institut Laue-Langevin (ILL) using a wavelength of $\lambda = 1.595072$ Å at both $T = 10$ and 298 K. The diffraction data were analyzed via Rietveld refinement using the FullProf Suite software.[72] The peak shape was modeled using the Thompson-Cox-Hastings pseudo-Voigt function, and a point-by-point background was subtracted. The following parameters were refined one by one: Scale factor, peak shape parameters, lattice parameters, atomic coordinates, individual anisotropic atomic displacement parameters and lithium occupancies. The zero-shift parameter was refined last, and any occupancies that resulted in unreasonable values were disregarded. Finally, all parameters were refined simultaneously to ensure stability of the calculated crystal structure.

*Magic-Angle Spinning Nuclear Magnetic Resonance Spectroscopy*: A Bruker Avance 500 MHz spectrometer was used for MAS NMR spectroscopy measurements with a magnetic field strength of 11.7 T, corresponding to resonance frequencies of 73.6, 99.4 and 202.5 MHz for $^6Li$, $^{29}Si$ and $^{31}P$, respectively. The samples were inserted into 2.5 mm rotors

under Ar atmosphere and subjected to spinning at a frequency of 30 kHz. The $\pi/2$ pulse length was 2.8 µs for $^6$Li, 1.8 µs for $^{29}$Si and 2.1 µs for $^{31}$P, while the recycle delay was set to 30 s for $^6$Li and 60 s for $^{29}$Si/$^{31}$P. The chemical shifts were referenced to 1 M $^6$LiCl for $^6$Li, tetramethyl silane for $^{29}$Si and $H_3PO_4$ (85%) for $^{31}$P.

*Transmission X-ray Absorption Spectroscopy*: Measurements were performed on a laboratory device (easyXAFS300+, easy XAFS LLC, Renton, WA, USA) based on Rowland-circle geometries. Pelletized samples were prepared inside an Ar-filled glovebox. Appropriate amounts of the $Li_{6.5}[P_{0.25}Si_{0.25}Ge_{0.25}Sb_{0.25}]S_5I$ (MC) and reference $GeS_2$ were diluted with cellulose and then pressed into 10 mm diameter pellets, which were further sealed by Kapton tape before being taken out from the glovebox. The Ge K-edge absorption spectra were measured using a Ge(555) spherically bent crystal analyzer (SBCA) and an Ag X-ray tube. An energy step of 0.25 eV was used for the X-ray absorption near edge structure (XANES) region and a step of 0.05 Å$^{-1}$ for the post-edge region (extended X-ray absorption fine structure, EXAFS). Multiple scans for each sample were performed to improve the signal-to-noise ratio and monitor the energy drift. The absorption spectra were calculated according to the transmission relation $\mu(E) \approx \ln(I_0/I_t)$ through a python-based software (easy XAFS LLC, Renton, WA, USA), which was also used for dead time correction. The reduced data were further processed and analyzed via the Demeter system.

*X-ray Photoelectron Spectroscopy*: XPS was applied to examine the differences in (surface) chemical composition of the different samples. The SE materials were transferred from the glovebox to the spectrometer (PHI 5000 VersaProbe equipped with a monochromatic Al $K_\alpha$ source, $h\nu = 1486.7$ eV) without exposure to air. The diameter of the illuminated area was 200 µm. Photoelectrons were collected with a pass energy of $E_{pass} = 23.5$ eV at three different electron escape angles, namely 20, 45 and 90° with respect to the surface normal. Because the SEs are poor electronic conductors, a neutralizer equipped with both a low-voltage electron gun and a floating ion gun generating a low-energy ion beam was used to compensate for sample charging. The binding energies are referenced to the C 1s photoelectron line of the C—C bond ($E_{bin} = 284.8$ eV). Fitting of the spectra was done as detailed in the literature.[36]

*Electrochemical Impedance Spectroscopy*: To measure the conductivity, pellets made from ≈200 mg of ball-milled precursor mixture were compressed at 3 t for 3 min in a 10 mm pellet die. They were then vacuum-sealed in quartz ampules ($10^{-3}$ mbar) and annealed for 10 h at 500 °C using the same synthetic procedure mentioned earlier. In electrodes (10 mm diameter) were attached on both sides of the pellets, and EIS was measured using a SP-200 potentiostat (BioLogic) with a 20 mV voltage amplitude from 0.1 Hz to 7 MHz. Spectra were collected in the temperature range from 15 to 65 °C after at least 1 h rest for equilibration. The conductivity was determined from the intercept with the x-axis, and the activation energy was calculated by linear fitting of the temperature-dependent conductivity using the Arrhenius equation. Residual porosity was not considered. For EIS on cold-pressed samples, ≈200 mg of powder was compressed in a customized setup with stainless steel dies and a PEEK sleeve (10 mm diameter) at 437 MPa for 3 min. A pressure of 250 MPa was maintained during the measurements.

*DC Polarization*: To determine the partial electronic conductivity, DC polarization measurements were performed at 25 °C by applying different voltages of 0.3, 0.4 and 0.5 V. Note that a similar setup as for EIS was used, and the measurements were conducted on sintered pellets. The resistance and the respective electronic conductivity were calculated from the steady-state current.

*Temperature-Dependent Pulsed Field Gradient Nuclear Magnetic Resonance Spectroscopy*: Temperature-dependent $^7$Li PFG NMR measurements were performed on a Bruker Avance 300 MHz spectrometer. The samples were enclosed in an evacuated 5 mm borosilicate glass tube, and a PFG probe with maximum gradient field strength of 30 T m$^{-1}$ was utilized. To suppress the effect of eddy currents, a stimulated-echo pulse sequence with bipolar gradients was employed.[73,74] Data were collected in the temperature range from 302 to 345 K. The $\pi/2$ pulse length was between 5.35 and 5.9 µs, and the recycle delay was 0.4–0.6 s. For all samples

and temperatures, gradient duration and diffusion time was 3 and 30 ms, respectively.

*Scanning Transmission Electron Microscopy*: Specimen preparation was done under Ar atmosphere in a glovebox (using a direct dispersion of the dry powders), and transfer to the microscope was accomplished using a Gatan inert transfer holder. The measurements were performed at 300 kV on a Themis 300 electron microscope with a DCOR probe corrector and Super X EDX detector.

*Electrode Preparation and Cell Assembly and Testing*: For SSB cells, the cathode composite was prepared by mixing LiNbO$_3$-coated NCM851005 (85% Ni, BASF SE) with the $Li_{6.5}[P_{0.25}Si_{0.25}Ge_{0.25}Sb_{0.25}]S_5I$ (MC) or $Li_6PS_5Cl$ SE (NEI Corp.) and Super C65 carbon black additive in a 69.3:29.7:1.0 weight ratio at 140 rpm for 30 min under Ar atmosphere using a 70 mL zirconia milling jar with 10 zirconia balls (10 mm diameter). The NCM851005 was heated for 2 h at 730 °C in O$_2$ flow to remove surface impurities, and the LiNbO$_3$ coating was prepared as reported in the literature.[75,76] The Super C65 carbon black was also dried at 300 °C in a dynamic vacuum overnight prior to use. For cell assembly, a customized setup with stainless steel dies and a PEEK sleeve (10 mm diameter) was used. First, ≈100 mg of SE was compacted at 62 MPa to form the SE separator layer. The cathode (≈13 mg) was then distributed onto the SE layer, and the stack was compressed at 437 MPa. Finally, an In anode (8 mm diameter, 125 µm thickness, Goodfellow) combined with a Li disc (3 mm diameter, 50 µm thickness, Albemarle) was attached to the other side of the separator layer. Galvanostatic testing was done at 25°C and under an external pressure of 81 MPa in the potential window of 2.28-3.68 V versus In/InLi (≈2.9-4.3 V versus Li$^+$/Li) after a resting period at open-circuit voltage (OCV) for 1 h using a MACCOR battery cycler. The C-rate was varied from 0.5 to 2.0C, with 1C = 190 mA g$_{NCM851005}^{-1}$.

*Cyclic Voltammetry*: SE and Super C65 carbon black were mixed at 140 rpm for 30 min under Ar atmosphere using a 70 mL zirconia milling jar with 10 zirconia balls (10 mm diameter). Cell assembly was done as described above, except that ≈13 mg of SE/Super C65 blend was used as working electrode (cathode). Scanning was done between 0.92 and 3.68 V versus In/InLi (≈1.54-4.3 V versus Li$^+$/Li) at 0.1 mV s$^{-1}$ and 25 °C after a resting period at OCV for 1 h using a SP-200 potentiostat (BioLogic).

*Statistical Analysis*: If not stated otherwise, all quantitative results reported in this paper are expressed as mean ± standard deviation.

## Supporting Information

Supporting Information is available from the Wiley Online Library or from the author.

## Acknowledgements

## Conflict of Interest

The authors declare no conflict of interest.

## Data Availability Statement

The data that support the findings of this study are available from the corresponding author upon reasonable request.

**ADVANCED
SCIENCE NEWS**

www.advancedsciencenews.com

**NANO · MICRO
small**

www.small-journal.com

[1] J. Janek, W. G. Zeier, *Nat. Energy* **2016**, *1*, 16141.

[2] J. T. Frith, M. J. Lacey, U. Ulissi, *Nat. Commun.* **2023**, *14*, 420.

[3] Y. Kato, S. Hori, T. Saito, K. Suzuki, M. Hirayama, A. Mitsui, M. Yonemura, H. Iba, R. Kanno, *Nat. Energy* **2016**, *1*, 16030.

[4] J. Janek, W. G. Zeier, *Nat. Energy* **2023**, *8*, 230.

[5] J. C. Bachman, S. Muy, A. Grimaud, H.-H. Chang, N. Pour, S. F. Lux, O. Paschos, F. Maglia, S. Lupart, P. Lamp, L. Giordano, Y. Shao-Horn, *Chem. Rev.* **2016**, *116*, 140.

[6] R. Chen, Q. Li, X. Yu, L. Chen, H. Li, *Chem. Rev.* **2020**, *120*, 6820.

[7] Z. Zhang, Y. Shao, B. Lotsch, Y.-S. Hu, H. Li, J. Janek, L. F. Nazar, C.-W. Nan, J. Maier, M. Armand, L. Chent, *Energy Environ. Sci.* **2018**, *11*, 1945.

[8] H.-J. Deiseroth, S.-T. Kong, H. Eckert, J. Vannahme, C. Reiner, T. Zaiß, M. Schlosser, *Angew. Chem., Int. Ed.* **2008**, *47*, 755.

[9] P. Adeli, J. D. Bazak, K. H. Park, I. Kochetkov, A. Huq, G. R. Goward, L. F. Nazar, *Angew. Chem., Int. Ed.* **2019**, *58*, 8681.

[10] X. Bai, Y. Duan, W. Zhuang, R. Yang, J. Wang, *J. Mater. Chem. A* **2020**, *8*, 25663.

[11] M. A. Kraft, S. Ohno, T. Zinkevich, R. Koerver, S. P. Culver, T. Fuchs, A. Senyshyn, S. Indris, B. J. Morgan, W. G. Zeier, *J. Am. Chem. Soc.* **2018**, *140*, 16330.

[12] L. Zhou, A. Assoud, Q. Zhang, X. Wu, L. F. Nazar, *J. Am. Chem. Soc.* **2019**, *141*, 19002.

[13] C. Yu, F. Zhao, J. Luo, L. Zhang, X. Sun, *Nano Energy* **2021**, *83*, 105858.

[14] S. Ohno, B. Helm, T. Fuchs, G. Dewald, M. A. Kraft, S. P. Culver, A. Senyshyn, W. G. Zeier, *Chem. Mater.* **2019**, *31*, 4936.

[15] L. Zhou, N. Minafra, W. G. Zeier, L. F. Nazar, *Acc. Chem. Res.* **2021**, *54*, 2717.

[16] S. Saha, G. Rousse, I. B. Alcover, M. Courty, D. A. Dalla Corte, J.-M. Tarascon, *Chem. Mater.* **2018**, *30*, 1379.

[17] C. A. Geiger, E. Alekseev, B. Lazic, M. Fisch, T. Armbruster, R. Langner, M. Fechtelkord, N. Kim, T. Pettke, W. Weppner, *Inorg. Chem.* **2011**, *50*, 1089.

[18] Y. Harada, T. Ishigaki, H. Kawai, J. Kuwano, *Solid State Ionics* **1998**, *108*, 407.

[19] A. Robertson, A. R. West, *Solid State Ionics* **1992**, *58*, 351.

[20] T. M. F. Restle, S. Strangmüller, V. Baran, A. Senyshyn, H. Kirchhain, W. Klein, S. Merk, D. Müller, T. Kutsch, L. van Wüllen, T. F. Fässler, *Adv. Funct. Mater.* **2022**, *32*, 2112377.

[21] F. Strauss, G. Rousse, D. Alves Dalla Corte, C. Giacobbe, R. Dominko, J.-M. Tarascon, *Inorg. Chem.* **2018**, *57*, 11646.

[22] H. Layer, M. G. Miller, L. Slifkin, *J. Appl. Phys.* **1962**, *33*, 478.

[23] L. K. Venkataraman, *Materials* **2021**, *14*, 2149.

[24] J. Hong, S. Kobayashi, A. Kuwabara, Y. H. Ikuhara, Y. Fujiwara, Y. Ikuhara, *Molecules* **2021**, *26*, 3559.

[25] A. Gautam, M. Sadowski, M. Ghidiu, N. Minafra, A. Senyshyn, K. Albe, W. G. Zeier, *Adv. Energy Mater.* **2021**, *11*, 2003369.

[26] S. Park, J.-W. Lee, *Korean J. Met. Mater.* **2021**, *59*, 247.

[27] A. Gautam, M. Sadowski, N. Prinz, H. Eickhoff, N. Minafra, M. Ghidiu, S. P. Culver, K. Albe, T. F. Fässler, M. Zobel, W. G. Zeier, *Chem. Mater.* **2019**, *31*, 10178.

[28] A. Behera, *In Advanced Materials: An Introduction to Modern Materials Science*, (Ed.: A. Behera), Springer International Publishing, Cham, **2022**, 291.

[29] C. Oses, C. Toher, S. Curtarolo, *Nat. Rev. Mater.* **2020**, *5*, 295.

[30] R.-Z. Zhang, M. J. Reece, *J. Mater. Chem. A* **2019**, *7*, 22148.

[31] Y. Ma, Y. Ma, Q. Wang, S. Schweidler, M. Botros, T. Fu, H. Hahn, T. Brezesinski, B. Breitung, *Energy Environ. Sci.* **2021**, *14*, 2883.

[32] A. Sarkar, Q. Wang, A. Schiele, M. R. Chellali, S. S. Bhattacharya, D. Wang, T. Brezesinski, H. Hahn, L. Velasco, B. Breitung, *Adv. Mater.* **2019**, *31*, 1806236.

[33] S.-K. Jung, H. Gwon, H. Kim, G. Yoon, D. Shin, J. Hong, C. Jung, J.-S. Kim, *Nat. Commun.* **2022**, *13*, 7638.

[34] Y. Zeng, B. Ouyang, J. Liu, Y.-W. Byeon, Z. Cai, L. J. Miara, Y. Wang, G. Ceder, *Science* **2022**, *378*, 1320.

[35] F. Strauss, J. Lin, M. Duffiet, K. Wang, T. Zinkevich, A.-L. Hansen, S. Indris, T. Brezesinski, *ACS Materials Lett.* **2022**, *4*, 418.

[36] J. Lin, G. Cherkashinin, M. Schäfer, G. Melinte, S. Indris, A. Kondrakov, J. Janek, T. Brezesinski, F. Strauss, *ACS Materials Lett.* **2022**, *4*, 2187.

[37] D. Bérardan, S. Franger, A. K. Meena, N. Dragoe, *J. Mater. Chem. A* **2016**, *4*, 9536.

[38] F. Strauss, J. Lin, A. Kondrakov, T. Brezesinski, *Matter* **2023**, *6*, 1068.

[39] Y. Li, S. Song, H. Kim, K. Nomoto, H. Kim, X. Sun, S. Hori, K. Suzuki, N. Matsui, M. Hirayama, T. Mizoguchi, T. Saito, T. Kamiyama, R. Kanno, *Science* **2023**, *381*, 50.

[40] S. Boulineau, M. Courty, J.-M. Tarascon, V. Viallet, *Solid State Ionics* **2012**, *221*, 1.

[41] C. Yu, L. van Eijck, S. Ganapathy, M. Wagemaker, *Electrochim. Acta* **2016**, *215*, 93.

[42] C. Yu, S. Ganapathy, E. R. H. van Eck, L. van Eijck, S. Basak, Y. Liu, L. Zhang, H. W. Zandbergen, M. Wagemaker, *J. Mater. Chem. A* **2017**, *5*, 21178.

[43] S. Harm, A.-K. Hatz, I. Moudrakovski, R. Eger, A. Kuhn, C. Hoch, B. V. Lotsch, *Chem. Mater.* **2019**, *31*, 1280.

[44] C. Dietrich, M. Sadowski, S. Sicolo, D. A. Weber, S. J. Sedlmaier, K. S. Weldert, S. Indris, K. Albe, J. Janek, W. G. Zeier, *Chem. Mater.* **2016**, *28*, 8764.

[45] R. Schlenker, A.-L. Hansen, A. Senyshyn, T. Zinkevich, M. Knapp, T. Hupfer, H. Ehrenberg, S. Indris, *Chem. Mater.* **2020**, *32*, 8420.

[46] F. Strauss, T. Zinkevich, S. Indris, T. Brezesinski, *Inorg. Chem.* **2020**, *59*, 12954.

[47] J. H. Song, Y. G. Choi, J. Heo, *J. Non-Cryst. Solids* **2006**, *352*, 423.

[48] Y. Lee, J. Jeong, H. J. Lee, M. Kim, D. Han, H. Kim, J. M. Yuk, K.-W. Nam, K. Y. Chung, H.-G. Jung, S. Yu, *ACS Energy Lett.* **2022**, *7*, 171.

[49] V. P. Zakaznova-Herzog, S. L. Harmer, H. W. Nesbitt, G. M. Bancroft, R. Flemming, A. R. Pratt, *Surf. Sci.* **2006**, *600*, 348.

[50] R. G. Avilez Garcia, C. A. Meza Avendaño, M. Pal, F. Paraguay Delgado, N. R. Mathews, *Mater. Sci. Semicond. Process.* **2016**, *44*, 91.

[51] J. H. Teo, F. Strauss, F. Walther, Y. Ma, S. Payandeh, T. Scherer, M. Bianchini, J. Janek, T. Brezesinski, *Mater. Futures* **2021**, *1*, 015102.

[52] Y. Ma, J. H. Teo, D. Kitsche, T. Diemant, F. Strauss, Y. Ma, D. Goonetilleke, J. Janek, M. Bianchini, T. Brezesinski, *ACS Energy Lett.* **2021**, *6*, 3020.

[53] J. Auvergniot, A. Cassel, J.-B. Ledeuil, V. Viallet, V. Seznec, R. Dedryvère, *Chem. Mater.* **2017**, *29*, 3883.

[54] F. Walther, R. Koerver, T. Fuchs, S. Ohno, J. Sann, M. Rohnke, W. G. Zeier, J. Janek, *Chem. Mater.* **2019**, *31*, 3745.

[55] R. Koerver, F. Walther, I. Aygün, J. Sann, C. Dietrich, W. G. Zeier, J. Janek, *J. Mater. Chem. A* **2017**, *5*, 22750.

[56] F. Walther, F. Strauss, X. Wu, B. Mogwitz, J. Hertle, J. Sann, M. Rohnke, T. Brezesinski, J. Janek, *Chem. Mater.* **2021**, *33*, 2110.

[57] J. Liang, X. Li, Y. Zhao, L. V. Goncharova, W. Li, K. R. Adair, M. N. Banis, Y. Hu, T.-K. Sham, H. Huang, L. Zhang, S. Zhao, S. Lu, R. Li, X. Sun, *Adv. Energy Mater.* **2019**, *9*, 1902125.

[58] D. Foix, D. Gonbeau, G. Taillades, A. Pradel, M. Ribes, *Solid State Sci.* **2001**, *3*, 235.

[59] D. A. Zatsepin, A. F. Zatsepin, D. W. Boukhvalov, E. Z. Kurmaev, N. V. Gavrilov, N. A. Skorikov, A. von Czarnowski, H.-J. Fitting, *Phys. Status Solidi B* **2015**, *252*, 2185.

[60] Y. Xu, K. Han, J. Xiang, X. Wang, *IEEE Access* **2020**, *8*, 159162.

[61] W. Zhang, T. Leichtweiß, S. P. Culver, R. Koerver, D. Das, D. A. Weber, W. G. Zeier, J. Janek, *ACS Appl. Mater. Interfaces* **2017**, *9*, 35888.

[62] A. Kuhn, V. Duppel, B. V. Lotsch, *Energy Environ. Sci.* **2013**, *6*, 3548.

[63] A. Kuhn, O. Gerbig, C. Zhu, F. Falkenberg, J. Maier, B. V. Lotsch, *Phys. Chem. Chem. Phys.* **2014**, *16*, 14669.

[64] S. J. Sedlmaier, S. Indris, C. Dietrich, M. Yavuz, C. Dräger, F. von Seggern, H. Sommer, J. Janek, *Chem. Mater.* **2017**, *29*, 1830.

[65] J. Maier, *Prog. Solid State Chem.* **1995**, *23*, 171.

[66] Y. Wang, H. Qu, B. Liu, X. Li, J. Ju, J. Li, S. Zhang, J. Ma, C. Li, Z. Hu, C.-K. Chang, H.-S. Sheu, L. Cui, F. Jiang, E. R. H. van Eck, A. P. M. Kentgens, G. Cui, L. Chen, *Nat. Commun.* **2023**, *14*, 669.

[67] P. Myagmarsereejid, M. Ingram, M. Batmunkh, Y. L. Zhong, *Small* **2021**, *17*, 2100241.

[68] B. Roy, B. R. Chakraborty, R. Bhattacharya, A. K. Dutta, *Solid State Commun.* **1978**, *25*, 937.

[69] F. Strauss, J. H. Teo, J. Janek, T. Brezesinski, *Inorg. Chem. Front.* **2020**, *7*, 3953.

[70] T. Shi, Y.-Q. Zhang, Q. Tu, Y. Wang, M. C. Scott, G. Ceder, *J. Mater. Chem. A* **2020**, *8*, 17399.

[71] F. Körmann, Y. Ikeda, B. Grabowski, M. H. F. Sluiter, *npj Comp. Mater.* **2017**, *3*, 36.

[72] J. Rodríguez-Carvajal, *Phys. B: Condens. Matter* **1993**, *192*, 55.

[73] K. S. Han, J. D. Bazak, Y. Chen, T. R. Graham, N. M. Washton, J. Z. Hu, V. Murugesan, K. T. Mueller, *Chem. Mater.* **2021**, *33*, 8562.

[74] W. S. Price, *Concepts Magn. Reson.* **1997**, *9*, 299.

[75] A.-Y. Kim, F. Strauss, T. Bartsch, J. H. Teo, T. Hatsukade, A. Mazilkin, J. Janek, P. Hartmann, T. Brezesinski, *Chem. Mater.* **2019**, *31*, 9664.

[76] S. Payandeh, F. Strauss, A. Mazilkin, A. Kondrakov, T. Brezesinski, *Nano Res. Energy* **2022**, *1*, e9120016.